# Active Range Imaging 2

This material is taken from the PhD-thesis:

*SIMD architectures for Range and Radar Imaging.*
*Linköping Studies in Science and Technology. Dissertations No.399.*

by Mattias Johannesson.

The material is chosen and scanned by Maria Magnusson Seger 2005-09-25.

# Chapter 1

# Introduction

## 1.1 Range Imaging

Normally, the image from a camera depicts the intensity distribution of the viewed scene as in the left image in Figure 1.1. A range camera on the other hand, depicts the distance from the camera to the objects of the scene as in the right image in Figure 1.1. In this range image the printed text is no longer visible, while the can opener and edges show up because of their difference in height. Interestingly, range and intensity images may also be combined as in Figure 1.2.

Range images are used in many applications, e.g. road surface surveying [9], industrial inspection [4], [50], [45], [65], and industrial robots [63]. In road surface surveys the goal is to measure cracks and ruts in the road surface. In industrial inspection the goals are often to determine if fabricated parts are within the tolerated sizes and/or orientations. In industrial robot applications we need to find locations and sizes of objects for navigation and/or object manipulation purposes.

Range images are obtained in many different ways. Traditionally these are separated into two categories, active and passive range imaging respectively. In active range imaging a dedicated and well defined light source is used in cooperation with the sensor. In passive range imaging no special light (except ambient) is required. The most common passive method is stereo vision where at least two images from different positions are used in a triangulation scheme. More detailed descriptions of different passive range imaging methods can be found in for instance [24], [1] and [22].

## 1.2 Active range imaging

Many active range imaging techniques use a *triangulation* scheme where the scene is illuminated from one direction and viewed from another. The illumination an-

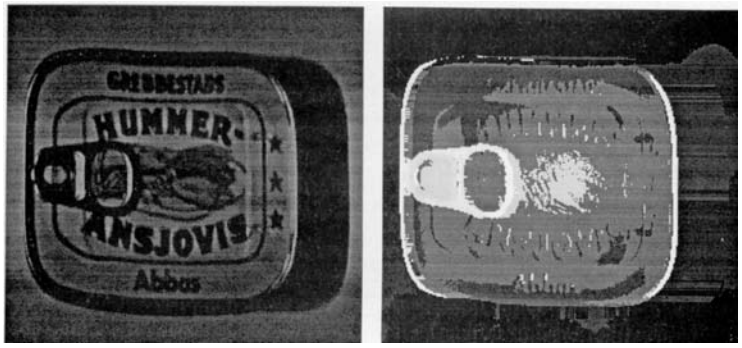


Figure 1.1: An intensity and a range image of a fish can. Dark areas are far away from the camera, and light areas close.

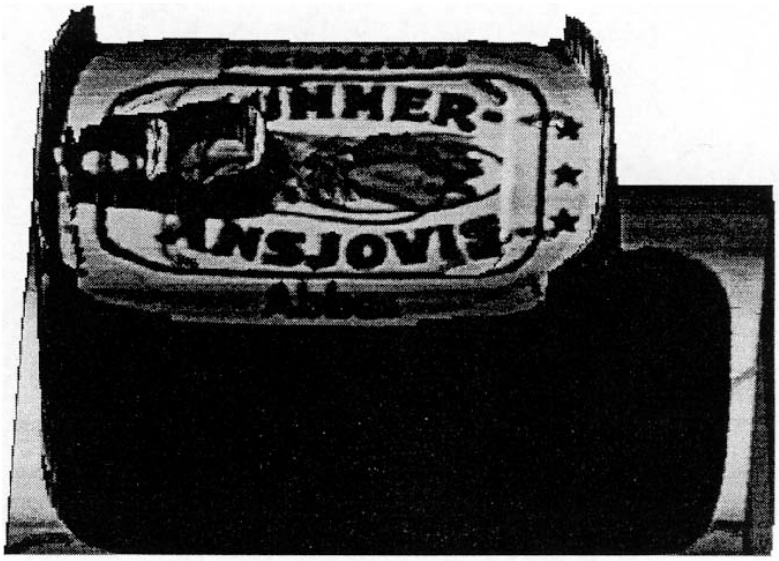

Figure 1.2: A combined range and intensity image.

gle, the viewing angle, and the baseline between the illuminator and the viewer (sensor) are the triangulation parameters. The most common active triangulation methods include illumination with a *single spot*, a *sheet-of-light* and *gray coded light*. A thorough discussion on the different methodologies can be found in for instance [64], [6] and [47]. The most common non-triangulation method is time-of-flight (radar), where the time for the emitted light pulse to return from the scene is measured. The high speed of electromagnetic waves makes time-of-flight methods difficult to use for high accuracy range imaging since small differences in range have to be resolved by extremely fine discrimination in time.

In single spot range imaging a single light ray is scanned over the scene and one range datum (rangel) is acquired for each sensor integration and position of the light, see Figure 1.3. Thus, in order to obtain an $M \times N$ image $M \times N$ measurements and sensor integrations have to be made. In sheet-of-light range imaging a sheet (or strip) of light is scanned over the scene and one row with $M$ rangels is acquired at each light position and sensor integration, see Figure 1.4. In this case only $N$ measurements and integrations are needed for an $M \times N$ image. Finally in a gray-coded range camera the scene is illuminated with $\log N$ gray coded patterns and therefore only $\log N$ integrations are needed to form one $M \times N$ image, see Figure 1.5.

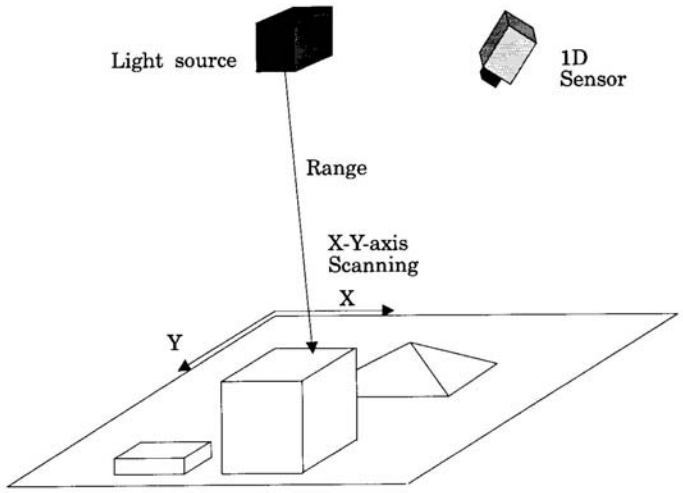


Figure 1.3: Single spot range imaging. Note that the range can also be defined as the distance between the sensor and the illuminated object instead of the distance between the light source and the object.

It would seem that the gray coded light method has speed advantages over the other active triangulation methods since fewer sensor integrations are needed.

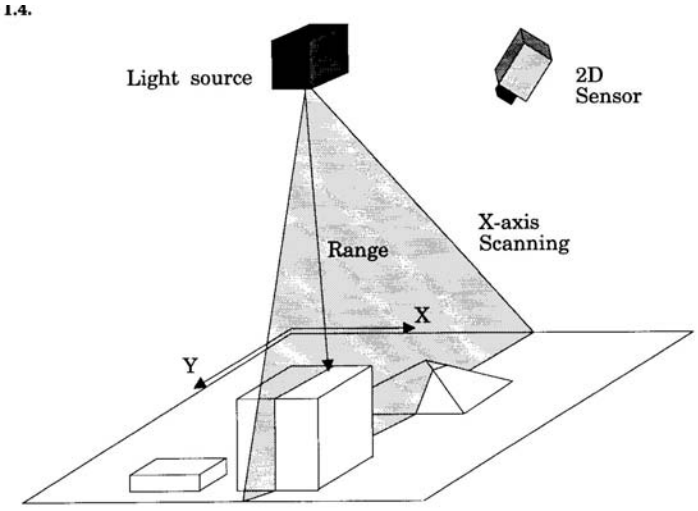


Figure 1.4: Sheet-of-light range imaging.

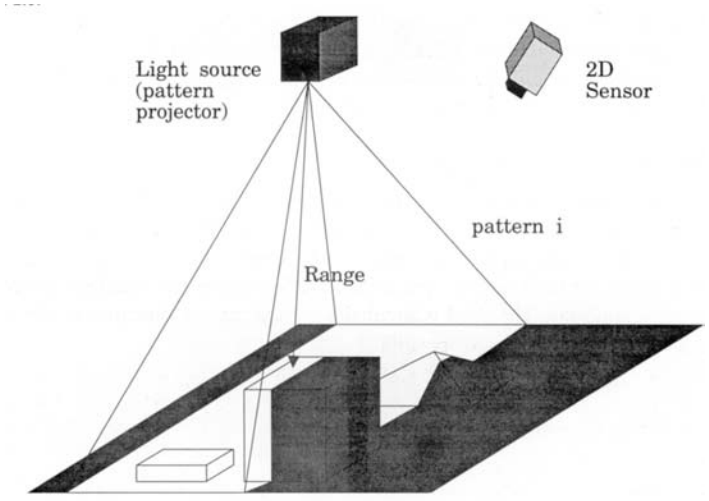


Figure 1.5: Range imaging with gray coded light.

However, one problem seems to be how to make a high intensity projector that can switch between patterns as fast as the sensor can integrate images. Hence, the trouble spot is the design of the illuminator rather than the sensor. Furthermore, any object movements between the integrations can give errors in the range image since the triangulation is performed *after* the $\log N$ integrations under the assumption that the illuminated scene was static. Admit tingly, the errors are minimized and not catas ophic due to the properties of the Gray code. In the other methods, however, each single sensor integration gives one set of range values. Therefore any object movement between integrations only gives a time dependent range image, where each range datum was correct when it was acquired.

In gray-coded light systems ordinary tungsten or halogen lamps are predominant instead of the laser light predominant in the other methods. We note that tungsten and halogen lamps are less harmful for the eyes than laser light and therefore better suited for measurements of human body parts.

The single spot technique requires advanced mechanics to allow the spot to reach the whole scene. At least two synchronous scanning mirrors are required. The advantage is that a relatively simple linear sensor, e.g. of the Position Sensitive Device type, can be used. But, the use of only one single sensing element often reduces the acquisition speed; the system presented by Rioux [49] reaches a rangel (range pixel) speed of 10 KHz. However, a recent system by the same research group actually outputs range data at RS-170 compatible video rate [5].

In the case of sheet-of-light systems, the projection of the light can be made with one single scanning mirror which is considerably simpler than the projector design for gray coded light, or the two mirror arrangement for single spot. Actually, in the sheet-of-light systems presented in this thesis the sheet-of-light is not swept at all. Instead the apparatus itself or the scene is moving. Thus, the camera system itself has no moving parts. In principle, however, the sensor designs to be presented are just as applicable to sweeping sheet-of-light.

Finally, it should be noted that a moving scene or moving apparatus rule out the gray-coded methods since they require a static scene during the $\log N$ integrations.

## 1.3 Sheet-of-light range imaging

In a sheet-of-light system range data is acquired with triangulation. The offset position of the reflected light on the sensor plane depends on the distance (range) from the light source to the object, see Figure 1.6. Using trigonometry we can solve the equations for the range if we know the distance between the laser and the optical center of the sensor (the *baseline*) and the direction of the transmitted ray. The third triangulation parameter, the direction of the incoming light ray, is

given by the sensor offset position.

For each position of the sheet-of-light the depth variation of the scene creates a contor which is projected onto the sensor plane, see Figure 1.6. If we extract the position of the incoming light for each sensor row we obtain an offset data vector that serves as input for the triangulations.

To make a sheet-of-light the pencil sharp laser spot-light passes through a cylindrical lens, see Figure 1.6. The cylindrical lens spreads the light into a sheet in one dimension while it is unaffected in the other. A sheet-of-light can also be made using a fast scanning mirror mechanism [4], an array of LED's [45], or with a slit projector [45].

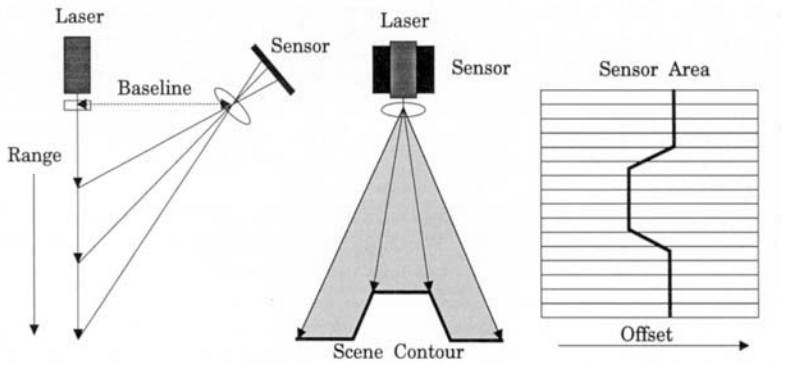


Figure 1.6: A range camera using sheet-of-light. Left: the illumination with the sheet-of-light perpendicular. Middle: parallel to the plane of the paper. Right: a snapshot of the sensor area.

As mentioned, two-dimensional range images can be obtained in at least three ways: by moving the apparatus over a static scene as in a road surface survey vehicle, by moving the scene as a conveyor belt, or by sweeping the sheet-of-light over a static 3D-scene using a mirror arrangement. In the two first cases the distance can be computed from the offset position in each row using a simple range equation or a precomputed lookup table. The third case is more awkward since the direction of the emitted sheet-of-light changes so that a second triangulation parameter becomes involved for each light sheet position.

In any case, for each illumination position and sensor integration, in the first processing step, the output from the 2D image sensor should be reduced to a 1D array of offset values.

Many commercial sheet-of-light range imaging systems are based on video-standard sensors. Such a sensor has a preset frame-rate, which in the PAL standard is specified as 50 Hz. This limits the range profile frequency to 50 Hz assuming

that the processing can be made in real-time. A $256 \times 256$ range image is then obtained in 5 seconds, and the range pixel frequency is 12.8 KHz. Even if the frame rate could be increased the sensor output is still serial which would require very high output and processing clock frequencies and possibly increase the noise level.

In [6] Besl reports on a few commercial sheet-of-light range imaging systems with CCD video-type sensors, but none of these have higher rangel frequencies than 5 KHz. As will be shown below, combining sensing and processing on the same chip implies that shorter integration times and considerably faster range imaging can be obtained.

# Chapter 2

# Optical design for sheet-of-light

## 2.1 Geometry definitions

In Figure 2.1 we show the coordinate system to be used in the sequel. The world coordinate system is $(X, Y, R)$ and the sensor coordinate system is $(S, T, A)$. The transformation between the coordinate systems can be described by two translations and one rotation (Translation $B$ along the X-axis, rotation $90 - \alpha$ around the $Y$-axis and translation $-b_0$ along the $A$-axis). As will be shown later, there might also be a skew of the $(S, T, A)$ system so that $A$ is non-orthogonal to the $(S, T)$ plane.

Since the $Y$ and $T$ axes are parallel, range measurements along the $R$-axis are independent of the sensor $t$-coordinate. This reduces all geometric range discussions to 2D, and we can view the system as in Figure 2.2 (for geometry definitions see Table 1). Here we only consider a non-scanning light-sheet and therefore the illumination angle $\gamma$ is set to $90^\circ$ unless otherwise is stated. This simplifies the range expressions somewhat. Also, the laser axis is considered vertical unless stated otherwise. A discussion on different scanning techniques can be found in [31].

| Word | Short | Definition |
|---|---|---|
| Optical center | $OC$ | Position of the center of the sensor system lens. |
| Optical axis | $OA$ | The $A$-axis, passing through the optical center. |
| Laser axis | $LA$ | Optical axis of the laser system (the $R$-axis). |
| Laser origin | $LO$ | Position along the laser axis closest to the optical center. Origin of world coordinate system. |
| Baseline | $B$ | Distance between the optical center and the laser origin. |
| View angle | $\alpha$ | Angle between the optical axis and the baseline. Also the angle between the laser sheet and the normal of the optical axis if $\gamma = 90°$. |
| Illumination angle | $\gamma$ | Angle between the baseline and the laser sheet. $90°$ unless deflected by a mirror. |
| Sensor angle | $\beta$ | Angle between the normal of the optical axis and the sensor $s$ axis. |
| Sensor position | $s, t$ | Sensor coordinates along rows and columns. Origin at optical axis. |
| Focal length | $f$ | Focal length of the lens. |
| Lens aperture | $d$ | Effective diameter of the lens. |
| Sensor distance | $b_0$ | Distance along the optical axis between the optical center and the sensor. |
| Focus distance | $a_0$ | Distance along the optical axis between the optical center and the sheet-of-light. |
| Range | $r(s)$ | Range (distance), parallel with the range axis, from $LO$ to a point in the laser sheet from where a ray emanates and hits the detector at s. $r(0) = R_0$ is the range of ray going in the optical axis. |
| Sensor height | $h_0$ | Height between the baseline-axis and the sensor center column position $(s = 0)$. |
| Sensor baseline | $b_{10}$ | The base in the triangle made by the optical axis, the sensor height and the baseline-axis. |
| Pixel pitch | $\Delta x$ | Inter-pixel distance on the sensor. |
| Sensor row size | $N$ | The number of pixels in a sensor row. |
| Light angle | $\rho$ | Angle between a light ray and the optical axis. |
| Max angle | $\rho_m$ | Maximum angular deviation from the optical axis. |
| Range interval | $R_T$ | Total range covered by light rays offset with $\lvert\rho\rvert < \rho_m$ from the optical axis. |

Table 1

Numerical examples are used in the sequel to give a better intuitive understanding of the problems and the derived equations. We consider two systems with equal view angles and approximately equal range interval but with different optics. One system utilize a "normal" lens with $f = 18$mm, the other one a "zoom" lens with $f = 75$mm. We also consider two apertures for each lens. The light sensitivity of a lens is expressed by the f-stop (relative aperture) $f/d$. The used f-stops are 5.4 and 1.8 which give the lens apertures 3.3 and 10mm for the 18mm lens and 14 and 42mm for the 75mm lens. Typical parameters are

| | | |
|---|---|---|
| Viewangle | $\alpha$ | $45^\circ$ |
| Range interval | $R_T$ | 500 mm |
| Sensor row size | $N$ | 256 |
| Pixel pitch | $\Delta x$ | 32 $\mu$m |
| Focal length | $f_1$ | 18 mm |
| Lens aperture | $d_A$ | 3.33 mm |
| Lens aperture | $d_B$ | 10.0 mm |
| Base line | $B_1$ | 520 mm |
| Focal length | $f_2$ | 75 mm |
| Lens aperture | $d_A$ | 13.9 mm |
| Lens aperture | $d_B$ | 41.67 mm |
| Base line | $B_2$ | 2282 mm |

Table 2

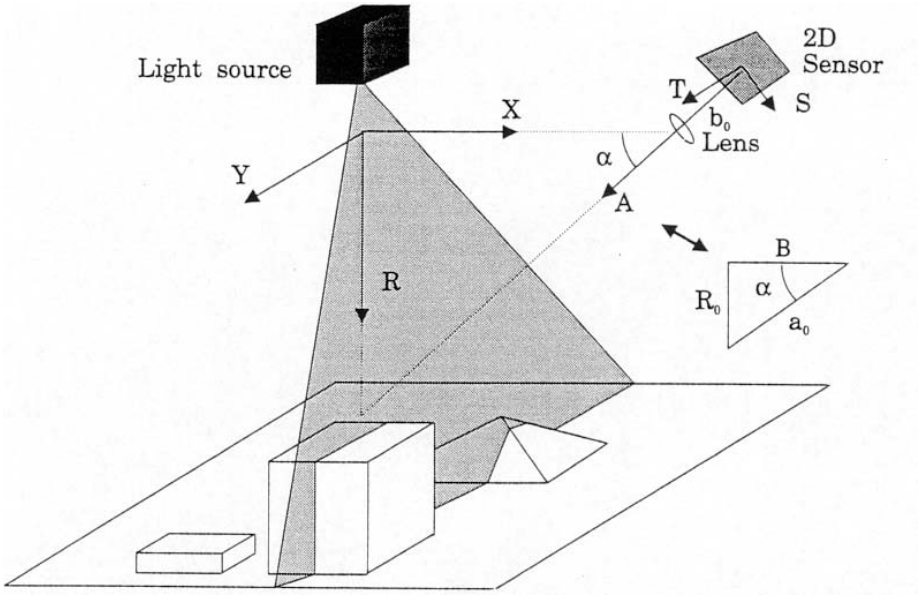


Figure 2.1: A sheet-of-light system with world and sensor coordinate system definitions.

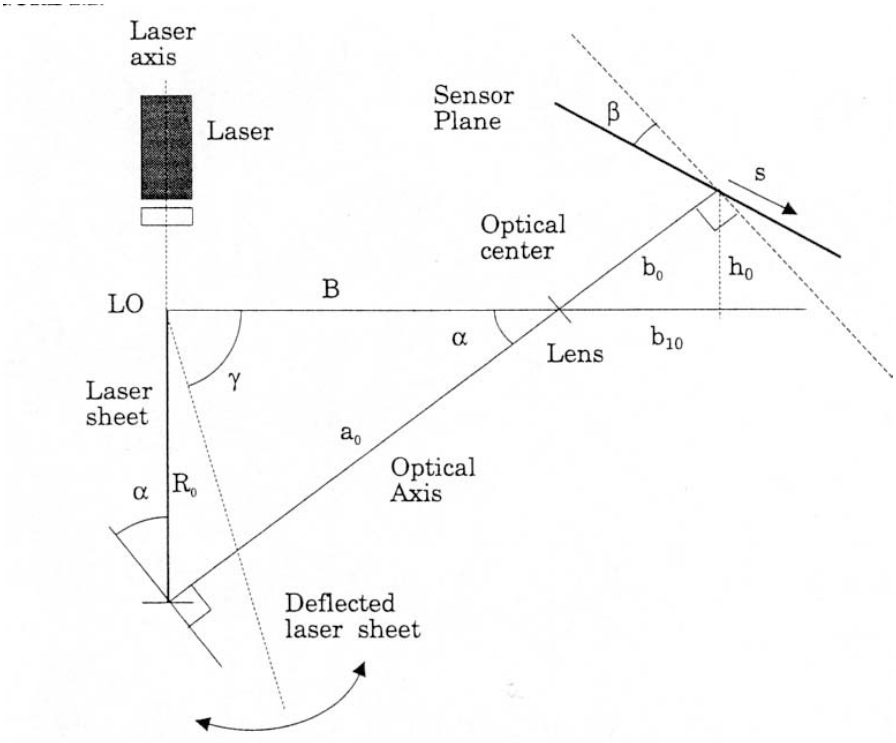


Figure 2.2: Illustrations to the definitions made in Table 1.

## 2.2 The Scheimpflug condition

In Figure 2.3 we see the sheet-of-light geometry for arbitrary laser and sensor angles, and for an arbitrary incoming light ray. The relation between the focal length and the sensor and focus distances is dictated by the lens law

$$\frac{1}{f} = \frac{1}{a_0} + \frac{1}{b_0} \tag{2.1}$$

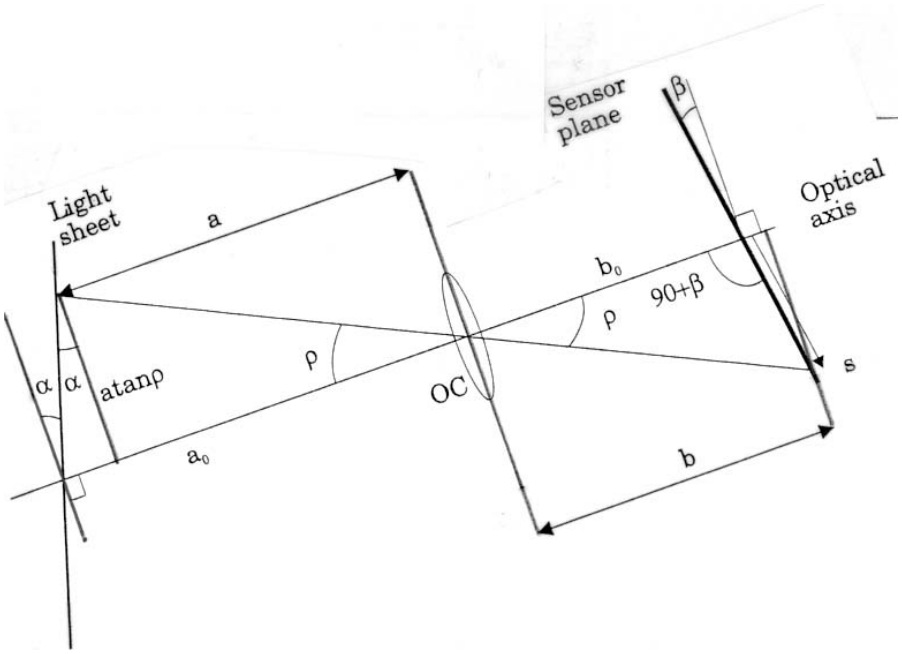


Figure 2.3: A setup with arbitrary sensor and laser angles and an ancoming light ray at and angle $\rho$.

For an arbitrary light ray making an angle $\rho$ with the optical axis and hitting the sensor at $s$, we can find the corresponding orthogonal distances $a$ and $b$ from the optical center to the laser sheet and the sensor. The equations are

$$a = \frac{a_0}{1 + \tan\rho \tan\alpha} \tag{2.2}$$

$$b = \frac{b_0}{1 - \tan\rho \tan\beta} \tag{2.3}$$

If we want the ray going to $s$ to be focused on the sensor plane, $a$ and $b$ must satisfy the lens law Equation (2.1). From Equation (2.2) and (2.3) we get

$$\frac{1}{a} + \frac{1}{b} = \frac{1}{a_0}(1 + \tan\rho\tan\alpha) + \frac{1}{b_0}(1 - \tan\rho\tan\beta) \tag{2.4}$$

$$= \frac{1}{f} + \tan\rho\left(\frac{\tan\alpha}{a_0} - \frac{\tan\beta}{b_0}\right) \tag{2.5}$$

We see that the lens law is satisfied for arbitrary angles $\rho$ if

$$\frac{\tan\alpha}{a_0} = \frac{\tan\beta}{b_0} \tag{2.6}$$

This is satisfied in the special case

$$\alpha = \beta = 0 \tag{2.7}$$

and in general for

$$\tan\beta = \frac{b_0\tan\alpha}{a_0} \tag{2.8}$$

The condition in Equation (2.7) implies that the sensor is orthogonal to the optical axis and that the optical axis is orthogonal to the laser axis. The condition in Equation (2.8) is known as the *Scheimpflug condition* [6], and defines the tilt of the sensor plane to achieve focus over the whole sensor plane on the sheet-of-light when the optical axis is not orthogonal to either plane. In normal cameras the sensor angle is fixed and orthogonal to the optical axis, which means that only the special condition in Equation (2.7) can be satisfied.

If we have a setup which satisfies the Scheimpfiug condition in Equation (2.8), how large is the angle $\beta$? Numerical examples are given in Table 3. As expected we find that $\beta$ is very small for view angles below say $70°$. Notice also that the angle is almost independent of the lens parameters for a given range interval and view angle.

| $f$ | $b_0$ | $\alpha$ | $\beta$ |
|---|---|---|---|
| 18 mm | 18.4 mm | $45°$ | $1.43°$ |
| 75 mm | 76.8 mm | $45°$ | $1.36°$ |
| 18 mm | 18.4 mm | $63°$ | $2.81°$ |
| 75 mm | 76.8 mm | $63°$ | $2.67°$ |
| 18 mm | 18.4 mm | $85°$ | $15.98°$ |
| 75 mm | 76.8 mm | $85°$ | $15.21°$ |

Table 3

As said before, in normal cameras the sensor plane is orthogonal to the optical axis and if we focus the camera on the light plane as in Figure 2.4 the focus condition in Equation (2.7) is satisfied. Unfortunately this arrangement is not very attractive. If we assume that the objects in the scene are planar and parallel with the optical axis, then when an object is higher than the range $R_0$ the laser light will by all likelihood be occluded, and no light will reach the sensor.

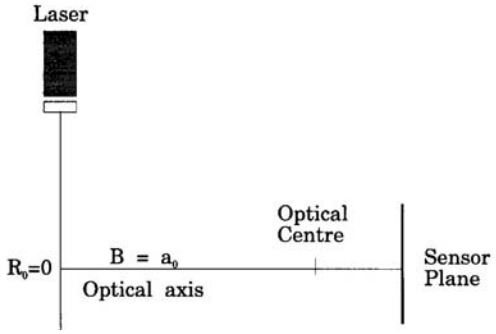


Figure 2.4: A system with the sensor aligned with the optical axis orthogonal to the light plane.

However, there might be applications where the surface orientations of the objects have little variation. The system in Figure 2.4 should then be arranged so that the object surface normal approximately bisects the $90^\circ$ angle between the laser sheet and the optical axis. For a case where the 3D scene moves horizontally the setup should be tilted $45^\circ$ as shown in Figure 2.5.

If we use the setup in Figure 2.4 but move the sensor so that the whole sensor is above the optical axis we still satisfy Equation (2.7). We then get the setup in Figure 2.6. However, normal lenses attenuate the intensity across the image plane with the factor $\cos^4 \rho$ [24]. Therefore, in Figure 2.6 where we utilize a shifted interval of the sensor plane off the optical axis, there is a price to pay in the form of uneven sensitivity along the sensor plane. Also, lenses are often less than ideal for light rays far away from the optical axis, which results in distorted images.

The most common arrangement for sheet-of-light systems is to tilt the camera and its optical axis so that the view angle $\alpha$ is substantially larger than zero, typically in the range of $30 - 60^\circ$, see Figure 2.6. This reduces the problem of occlusion, but the conditions in Equation (2.7) or (2.8) are not satisfied. Furthermore, the linearity found between range $r$ and sensor position $s$ in the previous cases is lost since linearity is only found when the sensor and laser planes are parallel. To regain linearity we can tilt the sensor as in Figure 2.5. Here, the sensor and view angles $\alpha$ and $\beta$ are equal but with opposite signs. Unfortunately this setup dissatisfies the conditions in Equation (2.7) and (2.8) even more, and

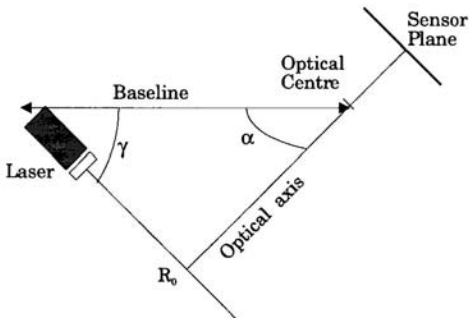


Figure 2.5: The system in Figure 2.4 tilted $45°$.

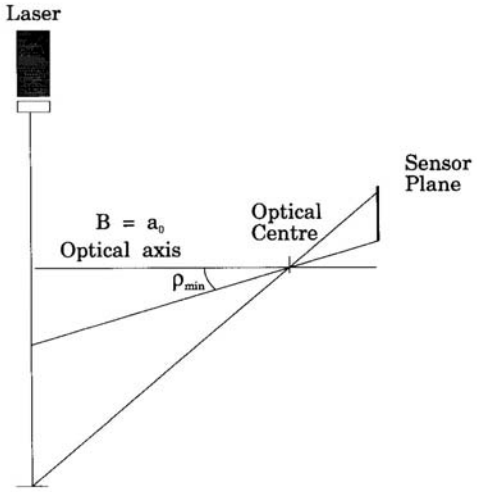


Figure 2.6: A system with the sensor offset from the optical axis.

therefore gives more unfocused (unsharp ) images. If we want a focused design we should use a setup as in Figure 2.7. but instead tilt the sensor according to the Scheimpflug condition in Equation (2.8).

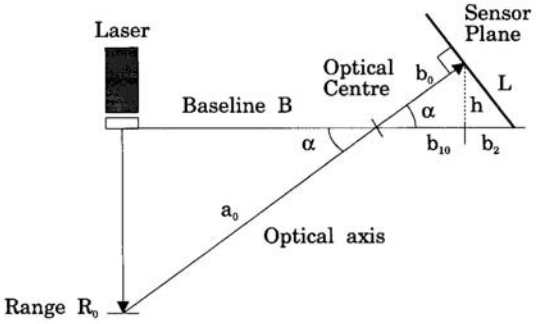


Figure 2.7: A system with the sensor aligned with the view-angle approximately $40°$.

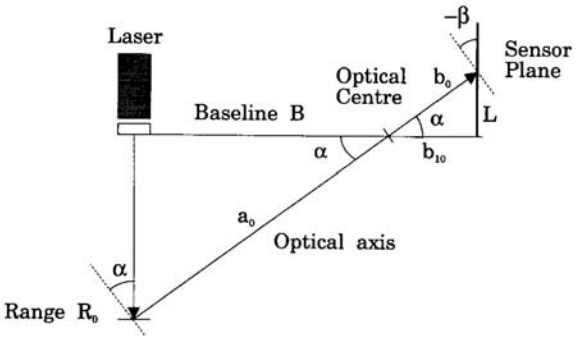


Figure 2.8: A setup for linearity between the sensor position and the range data.

## 2.3 Equations for range

From Figure 2.2 we have

$$R_0 = \frac{Bh_0}{b_{10}} \tag{2.9}$$

For an arbitrary light ray, offset from the optical axis with an angle $\rho_s$ and hitting the sensor at $s$, we get the geometry in Figure 2.9 where

$$r = \frac{Bh}{b_1} \tag{2.10}$$

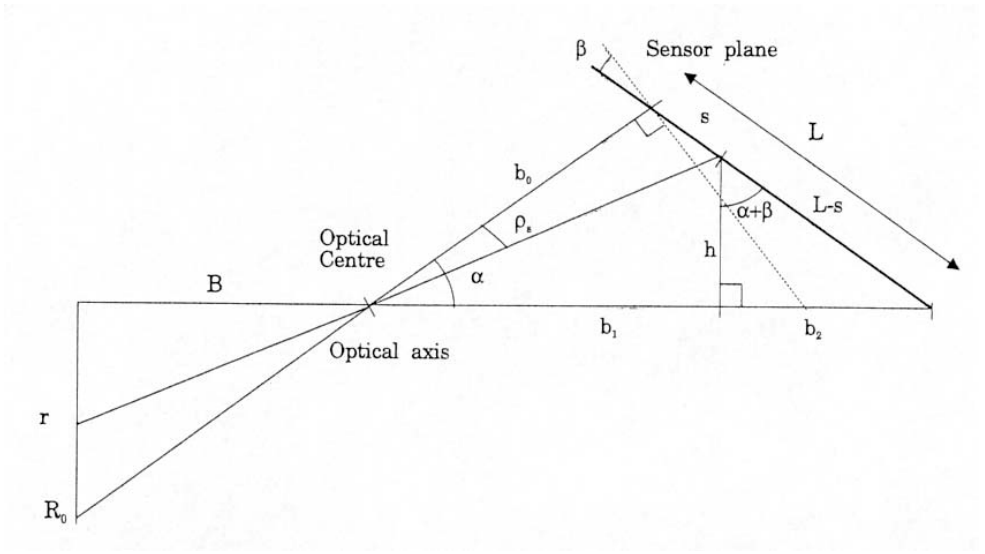


Figure 2.9: Geometry for an arbitrary sensor alignment, and an arbitrary input ray.

The geometry for the triangles give

$$b_1 + b_2 = \frac{b_0 \sin(90^\circ + \beta)}{\sin(90^\circ - (\alpha + \beta))} = \frac{b_0 \cos\beta}{\cos(\alpha + \beta)} \tag{2.11}$$

$$L = \frac{b_0 \sin\alpha}{\sin(90^\circ - (\alpha + \beta))} = \frac{b_0 \cos\beta}{\cos(\alpha + \beta)} \tag{2.12}$$

$$h = (L - s)\cos(\alpha + \beta) \tag{2.13}$$

$$b_2 = (L - s)\sin(\alpha + \beta) \tag{2.14}$$

Using Equation (2.11)-(2.14) in (2.10) yields

$$r = \frac{B\left(\frac{b_0 \sin\alpha}{\cos(\alpha+\beta)} - s\right)\cos(\alpha + \beta)}{\frac{b_0 \cos\alpha}{\cos(\alpha+\beta)} - \left(\frac{b_0 \sin\alpha}{\cos(\alpha+\beta)} - s\right)\sin(\alpha + \beta)} \tag{2.15}$$

This rather cumbersome equation holds for all sensor and laser alignments including the Scheimpflug geometry. For the special geometry in Figure 2.4 we have $\alpha = \beta = 0$, which simplifies Equation (2.15) to

$$r = \frac{-Bs}{b_0} \tag{2.16}$$

For the geometry in Figure 2.7 we have $\beta = 0$, which reduces Equation (2.15) to

$$r = \frac{B(b_0 \tan\alpha - s)\cos\alpha}{\frac{b_0}{\cos\alpha} - (b_0 \tan\alpha - s)\sin\alpha} = B\frac{b_0 \tan\alpha - s}{b_0 + s\tan\alpha} \tag{2.17}$$

For the geometry in Figure 2.8 we have $\alpha = -\beta$, which gives the range equation

$$r = \frac{B(b_0 \sin\alpha - s)}{b_0 \cos\alpha} \tag{2.18}$$

As mentioned above the most common setup is the one in Figure 2.7, with the non-linear range Equation (2.17). The non-linearity means that a constant precision $\Delta s$ in the sensor position $s$ results in a variable precision $\Delta r$.

## 2.4 Equations for width

In Figure 2.10 we see the correspondence between sensor coordinate $t$ and world coordinate $y$ which can be expressed as

$$y = -\frac{a \cdot t}{b} \tag{2.19}$$

where $a$ and $b$ as functions of $\rho$ are defined in Equation (2.2) and (2.3) and as shown in Figure 2.11 $\tan\rho$ is found using

$$\tan\rho = \frac{s\cos\beta}{b_0 + s\sin\beta} \tag{2.20}$$

If we combine these equations we obtain

$$y = \frac{-t \cdot B}{\cos\alpha(b_0 + s\sin\beta)\left(1 + \frac{s\cos\beta\tan\alpha}{b_0 + s\sin\beta}\right)} \tag{2.21}$$

If $\beta = 0$ Equation (2.21) can be simplified to

$$y = \frac{-t \cdot B}{b_0\cos\alpha\left(1 + \frac{s\tan\alpha}{b_0}\right)} = \frac{-t \cdot B}{b_0\cos\alpha + s\sin\alpha} \tag{2.22}$$

From Equation (2.21) and (2.22) it is evident that $y$ decreases for increasing $s$ and constant $t$.

As we have shown the range $r$ and width $y$ can be determined from the sensor offset position $(s, t)$ if we know the system parameters. However, in practice

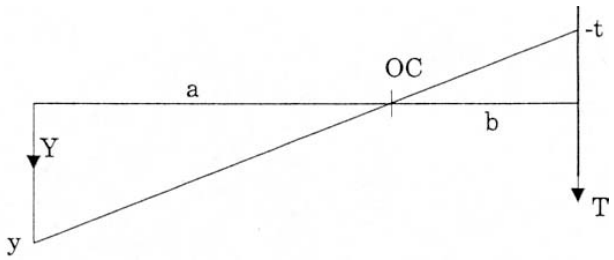


Figure 2.10: The width geometry.

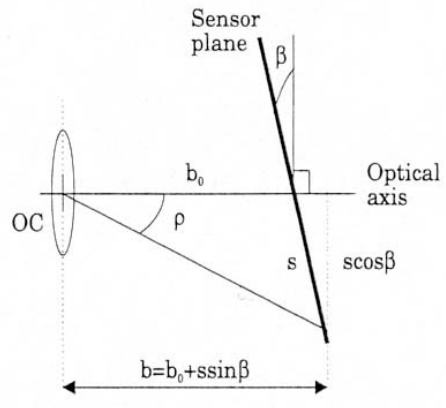


Figure 2.11: The focus distance as a function of the incoming light angle $\rho$.

these range equations are not often used to obtain the range in a sheet-of-light range imaging system. Instead the range values $(r, y)$ and their corresponding offset values $(s, t)$ are registered in a calibration procedure, and stored in a look-up table which later can be addressed with the sensor offset positions. The advantage of the calibration solution is that it may automatically compensate for lens and sensor aberrations [55] which are not accounted for in the formulas above. Sheet-of-light range camera calibration is discussed in chapter 3. Nevertheless, the Equations (2.15) - (2.22) should give a solid qualitative understanding of the design problems for sheet-of-light based ranging systems.

## 2.5 Accuracy limitations

Figure 2.12 gives an example of what happens with a laser sheet which is thicker than one pixel. We see that the range values are incorrect where the maximum intensity change to/from very low values. When one part of the laser sheet illuminates an area of low reflectance and the other part illuminates an area of high reflectivity the maximum intensity along the sensor row gets shifted left or right away from the center-plane of the sheet as shown in Figure 2.13. Off course, if the object refletivity is constant a wider laser sheet can be used and therefore the offset position can be obtained with very fine sub-pixel accuracy, see section 4.1.

Another problem with a thick laser sheet is the risk for multiple reflectIons when the laser illuminates two different ranges.

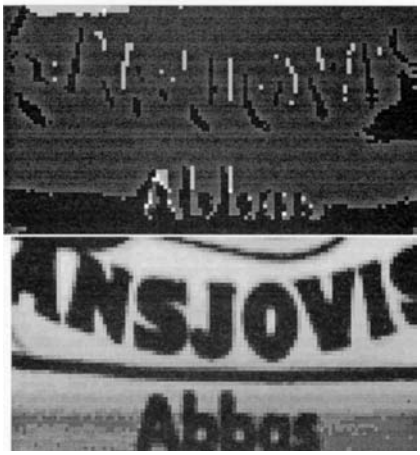

Figure 2.12: A range image where the laser sheet width is large. This range image depicts a flat surface. The top image is the range and the bottom is the intensity.

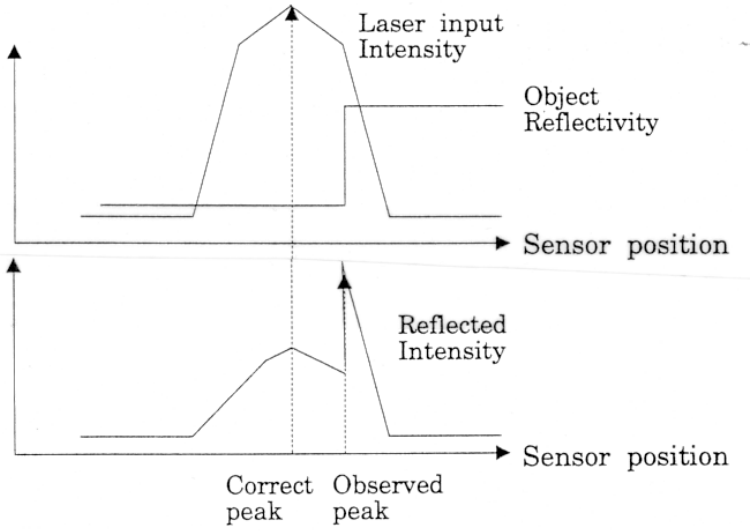


Figure 2.13: Response from a thick laser sheet illuminating an object with strong reflectivity contrast.

In theory the laser can be focused to a very thin sheet, limited only by the wavelength of the light. Unfortunately, some materials such as plastics spread the light so that a thick line is reflected nevertheless. If the 3D-object is made of a material which does not spread the light the potential range increment $\Delta r$ may well be in the $20\mu m$ range [45].

Since the laser sheet thickness changes over the range it is not possible to focus the laser precisely over a very large distance. In [44] dynamic laser focusing is suggested, but this requires that two range images are acquired. The first one is to achieve approximate range values so that the laser sheet focus distance can be adjusted and the second one to obtain the exact range.

## 2.6 Occlusion

A major problem in all triangulation methods is occlusion. In our case the problem manifests itself as one of the two following cases, see Figure 2.14. Either the laser light does not reach the area seen by the camera (laser occlusion) or the camera does not see the area reached by the laser (camera occlusion). In both cases the maximum reflection peak found in the sensor row data is the result of noise and/or ambient light. Any range value computed from such a maxima is totally insignificant as seen in Figure 2.15. We see large spurious range values

computed for a large occluded area to the right of the can and smaller occluded areas around the other edges.

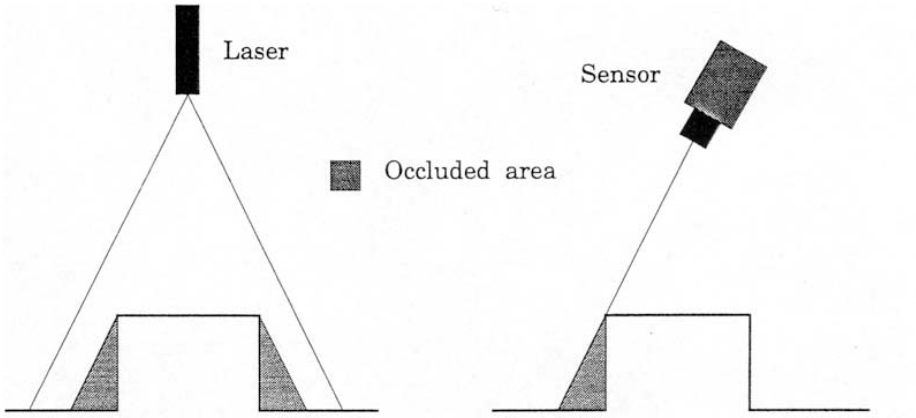


Figure 2.14: Laser (left) and camera (right) occlusion.

Both laser and camera occlusion can be minimized by careful placement of the laser and sensor. Laser occlusion is avoided by assuring that the laser reaches all areas seen by the sensor. Ideally, the baseline should be small so that the sensor and the laser can be considered as being in the same plane. Laser occlusion is then avoided by ensuring that the optical centre of the laser lens is further away from the scene than the optical centre of the sensor system, see Figure 2.16. Here the divergent sheet-of-light reaches all areas seen by the sensor since for any occluding object edge the area not illuminated by the laser is smaller than the area not seen by the sensor. Laser occlusion can also be avoided with multiple laser sources each illuminating the scene a little from the side, see Figure 2.17.

Sensor occlusion occurs when the baseline increases from the ideal zero value. This can only be avoided using multiple sensors as seen in Figure 2.18. If two sensors are used, each viewing with a baseline $B$, but from separate sides of the laser most of the sensor occlusion is avoided. For more on the problems and benefits of a two-sensor system see for instance [51]. The only remaining sensor occlusion comes from deep holes where both sensors are occluded [57]. The system can be designed with only one sensor and mirrors reflecting the light from two virtual baselines as in Figure 2.19 [43]. The sensor must alternate between imaging as the two virtual sensors since the sensor offset position will be different for the different virtual sensors. This technique also reduces the physical width of the system since the utilized baseline is wider than the system.

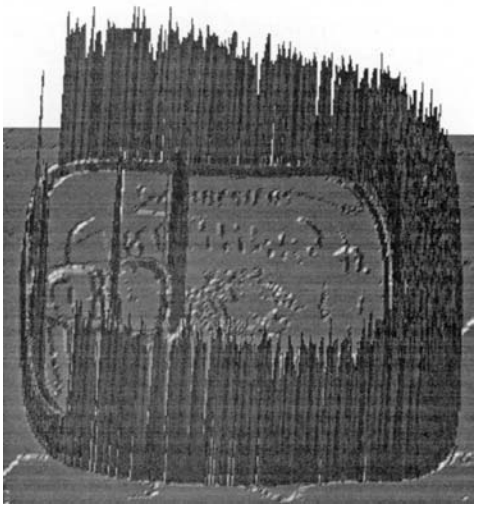

Figure 2.15: A 3D plot of an unfiltered range image of a fish conserve can illustrating the effects of occlusion.

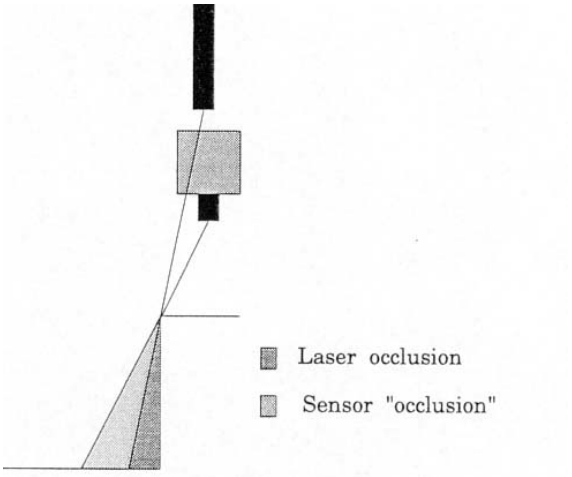


Figure 2.16: Laser occlusion avoidance.

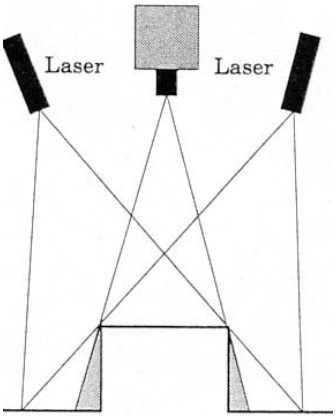


Figure 2.17: Laser occlusion avoidance using two lasers.

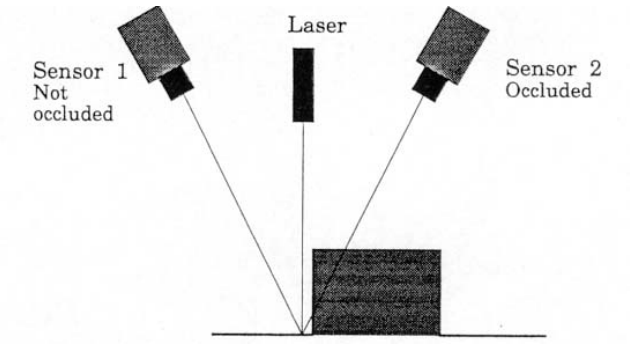


Figure 2.18: Sensor occlusion avoidance using two sensors.

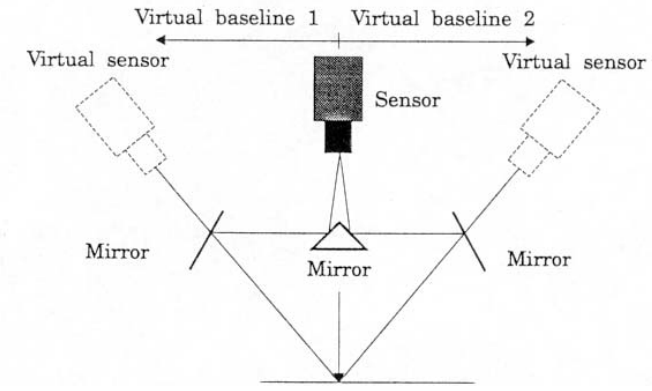


Figure 2.19: Using one sensor with two virtual baselines.

# Chapter 3

# Sheet-of-light range camera calibration

## 3.1 Calibration Procedures

As was shown in chapter 2 the mapping from sensor to world coordinates can be found using trigonometric and geometric calculations. Often the geometry parameters are hard to measure, especially the interior camera parameters, which are the focal distance and sensor center offset position relative to the optical center. An alternative to setup measurements is to calibrate the system to find all unknown parameters in the equations. No direct (non-iterative) solution exists to find all the parameters, only iterative solutions [23]. However, a direct (non-iterative) solution exists to find $4 \times 4$ homogenous transformation matrix describing the sensor-to-world transformation [51], [55]. Alternatively, if the interior camera parameters are known all transformation parameters in the equations can be determined [41].

Another approach is to find the precise matching for a number of points in the scene and make an interpolation for all points in-between [57]. This method takes all lens and setup distortions into account, but it is often cumbersome, both in data acquisition and in the mapping from sensor to world coordinates. If this mapping is made as a direct lookup, a table with $M \times N$ entries is needed. A smaller table can be used, but then a 2D interpolation step is needed for each 3D value that is computed. For example, if $N = 256$ and $M = 512$ a complete table with 32-bit data precision would require 1Mb.

A third approach, which is used here, is to calibrate the system and find a polynomial approximation of the desired functions for range and width derived in chapter 2. This approach results in two small 1D lookup tables (one with $N$ and one with $M$ values) and requires only two table lookups and one multiplication to

find the desired world coordinates for range and width. Another reason to choose this approach is that the resulting tables can be used with the existing *RANGER* range camera software [48]. However, this calibration scheme does not account for lens and setup distortions.

# Chapter 4

# Signal processing for sheet-of-light

## 4.1 Localizing the impact position on the sensor

Assume that the scene contour is reflected vertically along the image array as to the right in Figure 1.6. Along a row in the sensor the sheet-of-light reflected from the 3D scene may produce a signal as in Figure 4.1. Various rules and algorithms may be formulated to derive a unique impact position (*pos*) from this 1D signal. The most natural may be to find the position of the maximum intensity. Alternatively, we can threshold the signal and find the mid position of the pixels above the threshold. Analog devices such as position sensitive devices (see section 5.1) measure the center-of-gravity of the incoming light and this can also be computed with ordinary pixel-based sensors.

As indicated in Figure 4.1. even if the signal is well-behaved, the localization of the maximum of a discrete and quantized signal might be ambiguous. Assuming that the signal maximum is flat in the interval $a \leq x \leq b$ the position (*pos*) would naturally be chosen as

$$pos = \frac{a+b}{2} \tag{4.1}$$

In some smart sensors [11], [38] the position is actually given as either $a$ or $b$ whichever is easier to compute. Obviously, this simplification is allowed only if it is ensured that the interval $b - a$ is small.

If we use thresholding the peak mid position is given by

$$pos = \frac{n+m}{2} \tag{4.2}$$

where $n$ and $m$ are the first and last positions with a pixel value above the threshold respectively, see Figure 4.1. For signal peaks with a width of an even number of pixels Equations 4.1 and 4.2 result in a position halfway between two pixel

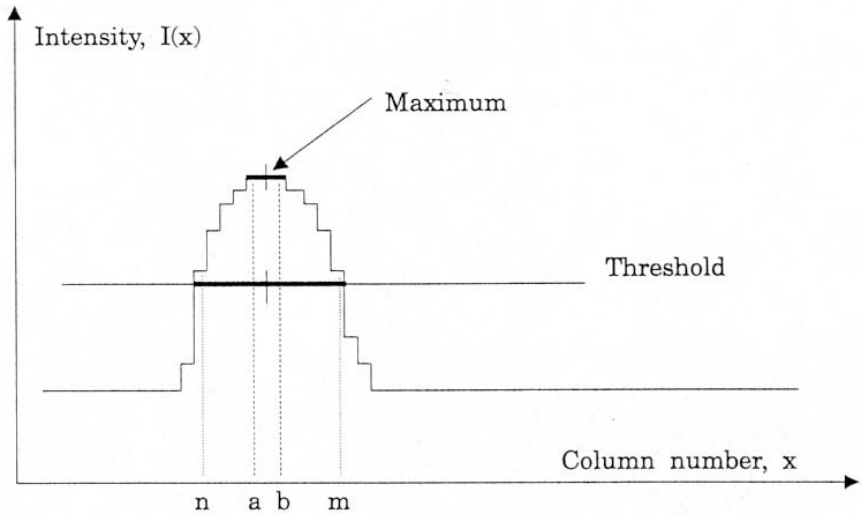


Figure 4.1: An illustration of two different ways to find the laser reflection.

centers. This tells us that these formulas give answers with half-pixel resolution (sub-pixel resolution).

The center-of-gravity position using the total signal is given by

$$pos = \frac{\sum_x xI(x)}{\sum_x I(x)} \tag{4.3}$$

where $x$ is the pixel column position and $I(x)$ the pixel intensity.

In [4] an accuracy of 1/20000 is claimed for a sensor with 388 pixels/row (which is 1/50 pixel sub-pixel resolution) using a White Scanner [54] with center-of-gravity computations. We find these claims somewhat doubtful and certainly impossible to hold up in the presence of noise and changing object reflectiveness. In [44 ] 1/16th of a pixel resolution is reported, but it is also stated that 1/2 pixel is a realistic value when viewing metallic surfaces with specular reflections. This resolution is acquired with a twin laser-sheet illumination scheme, and approximating (fitting) the signal bolus ( c.f. the signal in Figure 4.1) with a Gaussian before the center-of-gravity computation. The double-sheet illumination design utilizes two lasers of slightly different wavelengths displaced slightly from each other and this scheme is used to avoid effects of abruptly changing object reflectiveness (c.f. Figure 2.17).

Both the maximum and center-of-gravity techniques can be combined with thresholding, so that only values above a threshold are considered in the computations. This makes the computations less sensitive to noise and background illumination. A compromise between center-of-gravity and thresholding, where

multiple thresholds are used and the pos value is chosen as the mean center-of-gravity of the binary peaks obtained in the thresholding, is suggested in [20]. Maximum finding can also be combined with multiple thresholds to increase the position resolution.

## 4.2 Multiple maxima consideration

With all the above algorithms we get problems if two or more maxima appear in one sensor row. The most natural scheme would then be to simply remove or disregard the range results, or mark them as uncertain. However, this is not possible in all sensors. Some sensors/algorithms output the position of one of the maxima [11], or the mid-position between the two [2], [60].

In some applications it is desirable not to discard the values but to read out the range values from several peaks on one row, and leave the decision on which datum is correct to the next computational level. The reason that several peaks occur might not always be background illumination noise but secondary reflections from the laser reflecting on specular or transparent surfaces. In those cases more global information is needed to distinguish between the correct and the false reflections [46].

## 4.3 Post processing

The main purpose of the post processing is to detect, remedy, or alleviate the effects of occlusion and multiple reflections. Of course the true offset position for an occluded position can never be obtained, but once detected it might be approximated and/or interpolated, for instance using so called normalized convolution [39]. Alternatively the range data can be labeled as occluded (uncertain). We have used two different cues to detect erroneous (occluded) peak positions. Error filtering uses the error value, which we define as the number of detected maxima (peaks) in the sensor row. If occlusion occurred, the background illumination should be almost homogeneous and thus the probability that several peaks are found is large. This filtering is also very effective for detecting multiple reflections. Thus, when the number of maxima are more than one we know that the range datum is unreliable. Another way to detect and alleviate effects of occlusion is to use only those sensor rows where some pixels has an intensity above a certain maximum value. We define this as intensity filtering. If the laser is occluded very little light reaches the sensor row and the maximum intensity is low. Actually, if we use a thresholding algorithm intensity filtering is an integral part of the algorithm. An alternative to intensity filtering is to use the intensity as a

confidence measurement in normalized convolution. When discussing different smart sensors and smart sensor implementations we will also discuss their ability for intensity and/or error filtering. Further discussion on different post processing techniques can be found in [31].

# Selected References

[1] Andersson (Gökstorp) M.J., *Range from Out-of-Focus Blur.,* Lic. Thesis. LIU-TEK-LIC1992:17, Linköping 1992.

[2] Araki K., Shimizu M., Noda T., Chiba Y., Tsuda Y., Ikegaya K., Sannomiya K., Gomi M., *A range.finder with PSD's,* Machine Vision and Applications, MVA '90, Tokyo 1990.

[4] Beeler T.E., *Producing Space Shuttle Tiles with a 3-D Non-Contact Measurement System,* In "Three-Dimensional Machine Vision" ed. by T Kanade, Kluwer Academic Publishers 1987.

[5] Beraldin J.A., Rioux M., Blais F., Cournoyer L., Domey J., *Registered intensity and range imaging at 10 mega-samples per second,* Optical Engineering 31 (1), pp 88-94, 1992.

[6] Besl P. J., *Active Optical Range Imaging Sensors,* Advances in Machine Vision, Ch. 1, Springer, 1988.

[9] Burke M. et. al., *RST, Road Surface Tester,* Report from OPQ systems, Linkoping 1991.

[11] Danielsson P.E., *Smart Sensors for Computer Vision,* Report No. LiTH-ISY-I-1096, Linkoping 1990.

[20] Garcia D. F., del Rio M. A., Diaz j. L., Fransisco j. S., *Flatness defect measurement systemfor steel industry based on a real-time linear-image processor,* Proc of IEEE/SMC'93, Le Touquet 1993.

[22] Gökstorp M., *Range Computation in Robot Vision,* Ph.D. Thesis No. XX, Linkoping, 1995.

[23] Haralick R.M., Shapiro L.G., *Computer Vision, Vol II,* Addison Wesley, 1993.

[24] Horn B. K. P., *Robot Vision,* MIT press 1986.

[31] Johannesson M., *Sheet-of-light Range Imaging,* Lic thesis No.404, LIU-TEK-LIC-1993:46, Linkoping, 1993.

[38] Kanade T, Gruss A, Carley L.R, *A Fast Lightstripe Rangefinding System with Smart VLSI Sensor,* Machine Vision for Three-Dimensional Scenes, Ed. H Freeman, Academic Press, 1990.

[39] Knutsson H., Westin C.F., *Normalized and differential convolution: Methods for interpolation and filtering of incomplete and uncertain data,* Proc of IEEE Computer Society Conf. on Computer Vision and Pattern Recognition, New York, 1993.

[41] Melen T., Sommerfelt A., *Calibrating Sheet-of-Light Triangulation Systems,* Proc of SCIA '95, Uppsala 1995.

[43] Moss J.P., McCane M., Fright W. R., Linney A. D., James D. R., *A three-dimensional soft tissue analysis of fifteen patients with Class II, Division I malocclusions after bimaxillary surgery,* Am. Jour. of Orthodontics and Dental Orthopedics, Voll 05, 1994.

[44] Mundy l.L, Porter G.B. III, *A Three-Dimensional Sensor Based on Structured Light,* In "ThreeDimensional Machine Vision" ed. by T Kanade, Kluwer Academic Publishers 1987.

[45] Nakagawa Y, Ninomiya T, *Three-Dimensional Vision Systems Using the Structured-Light Methodfor Inspection Solder Joints and Assembly Robots,* In "Three-Dimensional Machine Vision" ed. by T Kanade, Kluwer Academic Publishers 1987.

[46] Nygårds J, Wernersson Å, *Gripping Using a Range Camera: Reducing Ambiguities for Specular and Transparent Objects,* Proc from Robotikdagar, Linköping 1993.

[47] Poussart D., Laurendeau D., *3-D Sensing for Industrial Computer Vision,* Advances in Machine Vision, Ch. 3, Springer, 1988.

[48] RANGER RS2200 *Technical Description,* IVP, Integrated Vision Products, Linkoping, 1994.

[49] Rioux M, *Laser Rangefinder based on synchronized scanners,* In "Robot sensors Voll Vision" ed. by A Pugh, Springer Verlag 1986.

[50] Rowa P., *Automatic visual inspection and grading of lumber,* Seminar Workshop on scanning technology and image processing on wood, Skellefteå, 1992.

[51] Saint-Marc P., Jezouin l.L., Medioni G., *A Versatile PC-Based Range Finding System,* IEEE Trans on Robotics and Automation, Vo17, No 2, 1991.

[54] Technical Arts Corp, *White Scanner 1OOa User's Manual,* Seattle, USA 1984.

[55] Theodoracatos V, Calkins D, *A 3-D Vision system Model for Automatic Object Surface Sensing,* In "Journal of Computer Vision", 11-1, pp 75-99, 1993.

[57] Trucco E., Fischer R. B., *Acquisition of Consistent Range Data Using Local Calibration,* Proc of IEEE Int Conf. on Robotics and Automation, San Diego, 1994.

[60] Verbeek P.W., Nobel l., Steenvoorden G.K., Stuivinga M., *Video-speed Triangulation Range Imaging,* NATO ASI Series, Vol F 63, pp 181-186, Springer-Verlag Berlin, Heidelberg 1990.

[63] Westelius C-J, *Preattentive Gaze Control for Robot Vision,* LIU-TEK-LIC-1992: 14,Linköping 1992.

[64] Ye Qin-Zhong, *Contributions to the Development of Machine Vision Algorithms,* Ph.D. Thesis No. 201, Linköping University 1989.

[65] Åstrand E., *Detection and Classification of Surface Defects in Wood. A Preliminary Study,* Report No. LiTH-ISY-I-1437, Linkoping 1992.

[66] Åstrand E., Johannesson M., Astrom A., Five contributions to the art of sheet-of-light range imaging, Report No. LiTH-R-ISY-1611, Linkoping, 1994.